

See discussions, stats, and author profiles for this publication at: <https://www.researchgate.net/publication/40022306>

# Coherent Oscillatory Femtosecond Dynamics in Multichannel Photodynamics of NO<sub>2</sub> Studied by Spatially Masked Electron Imaging

ARTICLE *in* THE JOURNAL OF PHYSICAL CHEMISTRY A · NOVEMBER 2009

Impact Factor: 2.69 · DOI: 10.1021/jp909031p · Source: PubMed

---

CITATIONS

7

---

READS

16

## 4 AUTHORS, INCLUDING:



**Daniel Irimia**

Delft University of Technology

11 PUBLICATIONS 97 CITATIONS

SEE PROFILE



**Ioannis D Petsalakis**

National Hellenic Research Foundation

142 PUBLICATIONS 1,590 CITATIONS

SEE PROFILE



**Maurice H M Janssen**

VU University Amsterdam

92 PUBLICATIONS 1,484 CITATIONS

SEE PROFILE

# Coherent Oscillatory Femtosecond Dynamics in Multichannel Photodynamics of NO<sub>2</sub> Studied by Spatially Masked Electron Imaging<sup>†</sup>

Daniel Irimia,<sup>‡</sup> Ioannis D. Petsalakis,<sup>§</sup> Giannoula Theodorakopoulos,<sup>§</sup> and Maurice H. M. Janssen<sup>\*‡</sup>

Laser Centre and Department of Chemistry, Vrije Universiteit, de Boelelaan 1083, 1081 HV Amsterdam, The Netherlands, and Theoretical and Physical Chemistry Institute, The National Hellenic Research Foundation, 48 Vassileos Constantinou Avenue, Athens 116 35, Greece

Received: September 18, 2009; Revised Manuscript Received: November 4, 2009

The femtosecond multiphoton photoionization and dissociation dynamics of NO<sub>2</sub> have been studied in a two-color pump–probe experiment at 400 and 266 nm using velocity map ion imaging in conjunction with photoelectron imaging. We report here a series of experiments focusing on the oscillatory patterns in pump–probe transients of the photoelectron signal. By using the technique of spatially masked imaging detection, we can select different photoelectron channels enabling the rapid measurement of energy selected transients with good signal-to-noise ratio. At short delay times (<300 fs) the dominant process is dissociative multiphoton ionization by  $3 \times 400 \text{ nm} + 1 \times 266 \text{ nm}$  excitation to a repulsive potential energy surface of the NO<sub>2</sub><sup>+</sup> cation correlating to NO<sup>+</sup>(<sup>1</sup>Σ<sup>+</sup>) + O(<sup>3</sup>P) and the ejection of a 0.37 eV electron. At longer delay times (>400 fs), the release of high-energy electrons (0.88 eV) is observed attributed to a three-photon absorption at 400 nm to Rydberg and valence type excited states of neutral NO<sub>2</sub> leading to predissociation and the production of NO<sup>+</sup> + O(<sup>3</sup>P) from a one-photon ionization at 266 nm. At longer delay times (>400 fs) a second slow (near 0 eV) photoelectron channel is observed that is associated with one photon excitation at 400 nm to the first excited  $\tilde{A}^2B_2$  state of NO<sub>2</sub> followed by two-photon excitation at 266 nm leading to near threshold ionization and dissociation to NO<sup>+</sup> + O(<sup>3</sup>P).

Distinctive oscillatory patterns were found in the pump–probe transients of the photoelectron yield for both the slow and the fast photoelectron channels but with different periods of about 750 fs (slow) or 590 fs (fast). Extensive polarization experiments are reported for both linear and circular polarized pump and probe laser geometries. We discuss the oscillatory mechanism in relation to ab initio calculations of relevant Rydberg and valence type excited states of NO<sub>2</sub> near 9.3 eV. We propose that an oscillating wavepacket of mixed Rydberg and valence character that predissociates is responsible for the observed oscillations in the transients of the fast (0.88 eV) photoelectron channel.

## I. Introduction

Over many years NO<sub>2</sub> has served as a benchmark molecule for frequency and time domain, theoretical and experimental studies of photophysical processes like dissociative ionization, unimolecular reaction dynamics, cluster dynamics, vibrational autoionization, state-to-state photoionization dynamics, vibronic coupling and non-Born–Oppenheimer dynamics. Even though at first glance NO<sub>2</sub> looks like a simple triatomic molecule, visible absorption and fluorescence spectra proved to be very complex and congested. The observed irregularities are mainly due to the presence of four low-lying interacting states. For instance vibronic coupling between the  $\tilde{X}^2A_1$  ground state and the first electronically excited  $\tilde{A}^2B_2$  state results in highly irregular and dense vibronic spectra in the region between 400 and 700 nm.<sup>1–3</sup>

Despite the fact that the spectroscopy of NO<sub>2</sub> has been widely studied in the frequency domain with narrow bandwidth continuous and pulsed nanosecond tunable laser sources, still recent time domain studies provide results which need further investigation and explanation. In experiments with femtosecond

laser pulses in either single color or two-color pump–probe configurations, the photodynamics of NO<sub>2</sub> have been studied by several groups over the past few years. In single color experiments with 50 fs pulses at 375 nm Singhal et al.<sup>4</sup> investigated NO<sub>2</sub> fragmentation and ionization. They attributed the formation of NO<sup>+</sup>(<sup>1</sup>Σ<sup>+</sup>) ions to fragmentation dynamics on the first electronically excited  $\tilde{A}^2B_2$  state which is strongly coupled to the electronic ground state  $\tilde{X}^2A_1$ . They proposed a one photon absorption and dissociation leading to ground state NO (<sup>2</sup>Π) which is subsequently ionized in a three photon absorption process. However, in subsequent time-resolved coincidence imaging studies by Hayden and co-workers<sup>5</sup> at the same laser wavelength of 375 nm but somewhat longer pulses of 120 fs duration, the authors attributed the formation of NO<sup>+</sup>(<sup>1</sup>Σ<sup>+</sup>) ions to a three-photon excitation to a highly excited repulsive state in NO<sub>2</sub>, correlating to NO(<sup>2</sup>Π) + O(<sup>3</sup>P), followed by dissociative ionization to form NO<sup>+</sup>(<sup>1</sup>Σ<sup>+</sup>). The multiphoton photodissociation dynamics of NO<sub>2</sub> were investigated by Schmidt et al.<sup>6</sup> who employed two-color pump–probe femtosecond excitation at 400 and 800 nm in combination with fluorescence depletion spectroscopy using strong (1–5 TW/cm<sup>2</sup>) laser pulse interaction. Their results were interpreted in terms of a mechanism involving strong field dressed states where nonadiabatic crossings of three dressed state potentials are

<sup>†</sup> Part of the “Benoît Soep Festschrift”.

<sup>\*</sup> Corresponding author, mhmj@chem.vu.nl.

<sup>‡</sup> Laser Centre and Department of Chemistry, Vrije Universiteit.

<sup>§</sup> Theoretical and Physical Chemistry Institute, The National Hellenic Research Foundation.

manipulated to enhance or suppress the fluorescence of NO ( $A^2\Sigma^+$ ,  $v = 0,1$ ) + O ( $^3P$ ).

More recently, a series of imaging experiments involving femtosecond pump–probe spectroscopy at 400 and 266 nm have studied the pathways responsible for the photofragmentation dynamics of NO<sub>2</sub>. One of the puzzling experimental observations by Whitaker, Soep, and co-workers was the presence of an oscillatory component in the pump–probe transient of NO<sup>+</sup> fragments and slow (near 0 eV) photoelectrons.<sup>7,8</sup> Initially, Eppink et al.<sup>7</sup> assigned these oscillations to the energy level spacing between coupled resonant levels in the mixed  $\tilde{A}^2B_2/\tilde{X}^2A_1$  states close to their conical intersection. On the contrary, the subsequent research by Form et al.<sup>8</sup> proposed that the origin of the slow NO<sup>+</sup> oscillating trace is a wavepacket motion along a soft coordinate with an energy level spacing of 40 cm<sup>-1</sup>, and they suggested that such a motion could be a free rotation of an oxygen atom around the core NO at large NO–O bond lengths. The low-frequency oscillations detected in the time domain spectra were debated in the theoretical study by Sanrey et al.<sup>9</sup> who launched wavepackets on the first excited electronic state and monitored the dynamical evolution of the system at times longer than 200 fs. Their calculations do not exclude the explanation by Form et al. that a free rotation of the oxygen atom around the NO core might be the cause of the presence of the oscillations. However, Sanrey et al. propose two alternative tentative explanations such that the oscillations might reflect the O–NO stretch (instead of oxygen rotation around NO) or they might originate from 1:2 resonances between symmetric stretch and bend vibrations at energies close to dissociation threshold.

Of special relevance to the oscillatory transients was the recent work of Vredenburg et al.<sup>10</sup> who used the powerful technique of femtosecond time-resolved photoelectron–photoion coincidence imaging.<sup>11</sup> They studied the NO<sub>2</sub> photofragmentation dynamics in a two-color pump–probe scheme with laser pulses centered at 400 and 266 nm. They provided very clear explanations and assignments of the different competing multiphoton channels leading to the formation of NO<sub>2</sub><sup>+</sup> or NO<sup>+</sup> cations and the various observed photoelectron channels. However, in the coincidence imaging study the oscillating transients were not addressed and no clear oscillatory patterns were measured most probably due to insufficient signal-to-noise ratio in the rather low-count rate coincidence study.

In this paper we want to provide a more detailed study on the coherent oscillations observed in the time evolution of the NO<sub>2</sub> multiphoton multichannel photodynamics using both photoion and photoelectron imaging spectroscopy, however, not in coincidence. In the present work we also employ a two color pump–probe excitation scheme at 400 and 266 nm and we focus especially on the transient photoelectron spectra. As known from the coincidence imaging study,<sup>10</sup> at long pump–probe delay times there are two kinds of electrons in coincidence with NO<sup>+</sup>, a first peak of electrons near zero kinetic energy and a second peak at a higher energy of 0.88 eV. This last electron peak was not observed by Whitaker and co-workers.<sup>7,8</sup> Here we present experimental data at various pump–probe laser polarization and very distinct but different oscillatory transients are observed in the two electron channels. In our study reported here we apply the technique of selectively masking the spatially sensitive imaging detector to discriminate photoelectrons of different energy. This masking technique of an imaging particle detector was first applied to ions by Chandler and co-workers,<sup>12</sup> and later on by others for threshold ions,<sup>13</sup> Doppler free detection of ions,<sup>14</sup> and the suppression of hot electrons in coincidence

spectroscopy.<sup>15</sup> From the analysis of our experimental and theoretical results we propose that a mechanism involving NO<sub>2</sub> Rydberg state potentials may cause the oscillating pattern in the transients. This paper is structured as follows. In section II we give a brief description of the experimental setup, in section III we present the various experimental data measured, and in section IV we discuss our proposed mechanism in combination with theoretical surface calculations of highly excited Rydberg states of NO<sub>2</sub>. Finally, we summarize our conclusions in section V.

## II. Experimental Section

The experimental setup that is used here was initially designed for velocity map ion imaging experiments<sup>16–18</sup> and was adapted in 2003 for femtosecond time-resolved photoelectron imaging studies.<sup>19</sup> The setup was recently also described in papers reporting a new technique to image with femtosecond lasers directly in situ the speed distribution of pulsed atomic and molecular beams produced by a novel piezo valve.<sup>20,21</sup> In this section we will just describe shortly the relevant working conditions for the present experiment. The supersonic molecular beam was prepared by seeding 2% NO<sub>2</sub> in helium and expanded through a 200  $\mu$ m diameter pulsed piezo nozzle operating at a repetition frequency of 1 kHz. The backing pressure behind the nozzle was kept low to a value of about 1 Bar in order to prevent the formation of clusters. The supersonic molecular beam expansion is collimated by two skimmers before entering the imaging chamber where it is intersected at a right angle by the femtosecond pump and probe laser beams. The interaction of the femtosecond pulses with the parent molecules leads to different ionization and dissociation processes. The ejected photoions or electrons are accelerated perpendicular to the plane determined by the molecular beam, and the laser pulses onto a position-sensitive detector consisting of a microchannel-plate (MCP) backed by a fast phosphor screen (P47) and charged-coupled-device (CCD) camera system. Two different MCPs were used over the course of the experiments, one MCP with pore diameter  $D = 5 \mu$ m, channel length  $L:D = 60:1$ , 40  $\mu$ m effective diameter chevron plates, and a second MCP with pore diameter  $D = 10 \mu$ m, Channel length  $L:D = 40:1$ , 42  $\mu$ m effective diameter chevron plates. For some of the experiments we selectively masked the fiber-optic output window of the imaging CCD detector<sup>12</sup> so that only light from a certain energetic photoelectron was transmitted, which was recorded by a sensitive photomultiplier tube (PMT). The differently produced photoelectrons have the same arrival time at the detection system but have different energy; i.e., they hit at different locations on the position-sensitive MCP detector. Hence, even though we cannot perform a time discrimination (gating), we are able to separate them spatially according to their energies. For that purpose we masked the detector by blocking the signal of undesired photoelectrons and detecting the signal from the selected energy range. In this way good transients with sufficient signal-to-noise ratio were obtained for selected photoelectron channels directly from the PMT output, facilitating enormously the measurement of the oscillations in the pump–probe transients of selected photoelectron channels.

Our experimental setup is capable of easily handling either the ion or the electron images; however, images are obtained separately as opposed to the correlated ion and electron images obtained in a coincidence imaging experiment.<sup>11</sup> The difference between ion and electron detection consists of a few modifications made to the setup and the detection method. In the case of ion imaging, positive voltages are applied on an electrostatic

lens system and the front plate of the MCP detector is negatively gated by a home-built fast rising HV-pulsar ( $\sim 15$  ns) with variable width (minimal 120 ns) in order to achieve mass selection. For electron detection, negative voltages are applied on repeller and extractor plates, the field-free region (36 cm) is shielded by a  $\mu$ -metal shielding tube placed tightly around the time-of-flight tube in order to avoid the external magnetic fields that might deflect the trajectories of the light electrons. The front MCP surface facing the TOF tube is held at ground potential while the back plate is gated by a different home-built fast positive pulser<sup>22,23</sup> with variable width applied over a constant bias of about 1000 V. Because the electric fields applied in our velocity map configuration can be varied in such a way that we can magnify and select the photoelectron images to any size, the pixel-to-energy calibration of the detector is needed for a specific set of voltages. The calibration factor can be theoretically calculated by having the mass and the measured time of flight of a specific detected fragment, but in the case of very light electrons for a high accuracy we imaged the xenon photoelectrons in the pump–probe configuration using 266 and 400 nm, respectively. The simplicity of the photoelectron images interpretation is due to well-known Xe<sup>+</sup>(<sup>2</sup>P<sub>3/2</sub>) and Xe<sup>+</sup>(<sup>2</sup>P<sub>1/2</sub>) ionic states separated by 1.31 eV.<sup>24,25</sup> The peaks in the spectrum are obtained by  $4 \times 400$  nm and  $3 \times 266$  nm ionization from the individual beams as well as combination of photons  $3 \times 400$  nm +  $1 \times 266$  nm and  $2 \times 266$  +  $1 \times 400$  nm and correlate to Xe<sup>+</sup>(<sup>2</sup>P<sub>3/2</sub>) and Xe<sup>+</sup>(<sup>2</sup>P<sub>1/2</sub>) ions.

The femtosecond laser consists of a commercial amplified regen laser system (Spectra Physics Spitfire) that produces a 1 kHz pulse train and is tunable around 800 nm with an output energy of about 800  $\mu$ J and a duration of 120 fs. Employing the frequency mixing technique, the 800 nm fundamental light is doubled and tripled in BBO crystals generating the pump and probe pulses centered at 400 and 266 nm, respectively. The pump beam is then sent via a delay line stage in order to introduce a variable optical path length and is subsequently recombined with the probe beam by a dichroic mirror. Both beams can be focused separately and are recombined collinearly into the molecular beam machine. The energies injected into the machine are typically 25–45  $\mu$ J/pulse at 400 nm and 5–7  $\mu$ J/pulse at 266 nm, but also pulses up to 60  $\mu$ J/pulse at 400 nm and 15  $\mu$ J/pulse at 266 nm were used occasionally. Polarization directions of the pump and probe lasers were usually set parallel to each other and parallel to the plane of the charged particle imaging detector. However, for the polarization studies we used also different polarization configurations in the experiments employing variable waveplates (Alphas) and polarizers.

### III. Results

**A. Overall Transients and Images.** In a two-color pump–probe excitation at  $\tau = 0$  fs using bandwidth-limited 266 and 400 nm laser pulses, the TOF mass spectrum shows two mass peaks, the largest peak is the NO<sup>+</sup> fragment ion, the smaller peak (about 15–35% depending somewhat on the laser individual pulse energies) is the NO<sub>2</sub><sup>+</sup> parent ion. In Figure 1a the pump–probe transient of the NO<sup>+</sup> fragment ion is shown as a function of the delay between 400 and 266 nm laser beams. Around  $\tau = 0$  fs there is a strong pump–probe enhancement, and at positive delay times (i.e., the 400 nm pump pulse is arriving before the 266 nm probe pulse) the NO<sup>+</sup> transient shows a pronounced oscillatory component with a period of about 600 fs. In Figure 1b the pump–probe transient of the total yield of photoelectrons is shown, and again at positive delay time similar oscillations are observed. Finally, in Figure 1c the pump–probe

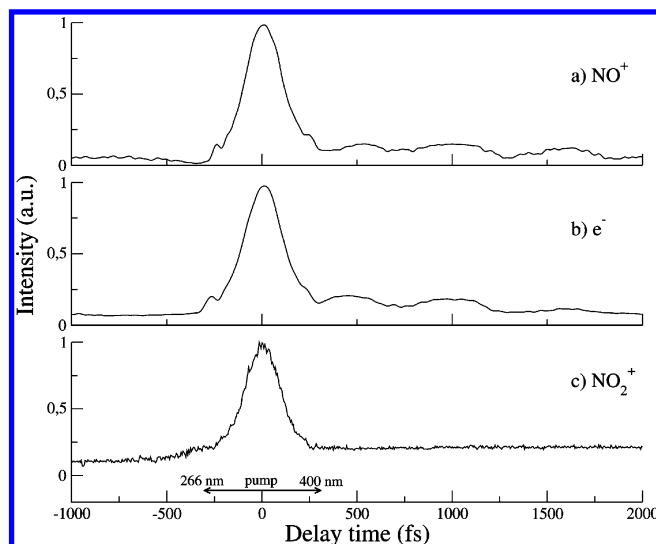


**Figure 1.** Temporal profile of the (a) NO<sup>+</sup> fragment ion, (b) total photoelectron signal, and (c) NO<sub>2</sub><sup>+</sup> parent ion recorded as a function of the delay of the probe pulses centered at 266 nm following excitation of NO<sub>2</sub> at 400 nm. The energies of the pump and probe pulses were 30 and 4  $\mu$ J, respectively.

transient of the NO<sub>2</sub><sup>+</sup> parent ion is shown, again a strong enhancement at  $\tau = 0$  fs; however, at positive delay time a small enhancement is observed without any oscillatory structure. As can be seen, the signal on the NO<sub>2</sub><sup>+</sup> parent ion is much noisier than the other two transients because the NO<sub>2</sub><sup>+</sup> parent ion is a much smaller ion signal as observed from the TOF mass spectrum.

In Figure 2 the two-dimensional (2D) projected velocity map photoelectron images are shown at three different pump–probe delay times: 0, 300, and 1000 fs. The average integration time used to record these velocity map electron images was usually about 5 min for each image. The contributions of the individual pump and probe laser pulses to the photoelectron images were subtracted from the pump–probe two-laser image by measuring an image at a time delay of about  $-1$  ps; i.e., the 266 nm pulse is before the 400 nm pulse. This background image is subtracted from the images at positive time delay. The polarizations of both the 400 nm pump and the 266 nm probe lasers were linear and parallel to each other and in the plane of the CCD detector. Because of the cylindrical symmetry of the electron distributions around the electric vector of the linearly polarized light, the original 3D scattering distributions can be reconstructed from the 2D projections by an inverse Abel transform. The angular integration of the Abel inverted 3D distribution as a function of the radial position gives the kinetic energy distribution of the electrons using the calibration of pixel-to-velocity at the particular ion optics voltages obtained from xenon photoelectron images. The resulting photoelectron energy distribution is shown at eight different pump–probe delay times in Figure 3.

The photoelectron kinetic energy spectra show a strong change with the delay time between the pump and the probe laser pulses. At short delay times (around 0–100 fs), the photoelectron spectra exhibit two peaks, one with an energy of  $\sim 0.37$  eV and another one at 1.45 eV. Around 200–300 fs the peak near 0.37 eV becomes weaker and two new peaks grow in, a photoelectron peak near 0 eV and an initially broader peak near 0.8–0.95 eV. At even longer delay times the peak near 0.88 eV sharpens up and does not seem to change shape beyond 800 fs or so.

The image of the parent NO<sub>2</sub><sup>+</sup> ion has no structure and is basically a small focused spot; therefore we do not show it here.



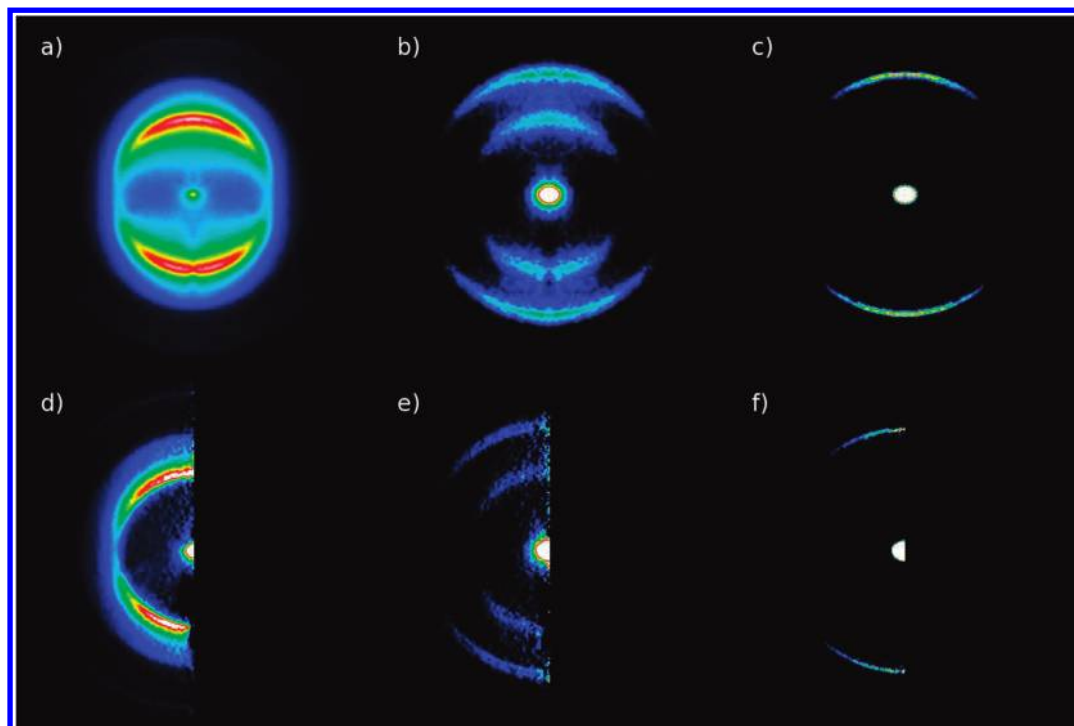


**Figure 2.** Top panels: photoelectron images of  $\text{NO}_2$  recorded at (a) 0 fs, (b) 300 fs, and (c) 1000 fs delay time between the 400 nm pump pulses and 266 nm probe pulses. Bottom panels (d–f): the corresponding Abel-inverted images.

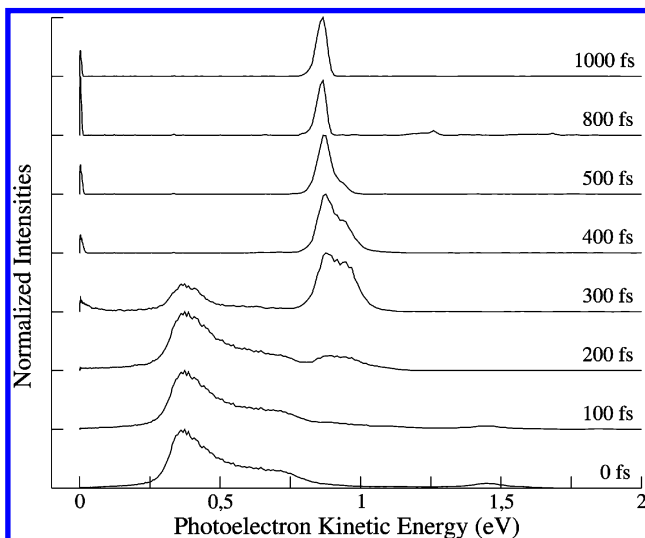


**Figure 3.** Time dependence of the photoelectron kinetic energy distribution obtained with 400 nm pump and 266 nm probe wavelengths. The spectra at 0, 300, and 1000 fs represent the radial energy distribution obtained from the images presented in Figure 2.

An example of the observed  $\text{NO}^+$  ion image at 0 fs pump–probe delay is shown in Figure 4a. From this image, the total translational energy distribution of the  $\text{NO}^+ + \text{O}$  channel can be extracted using conservation of linear momentum between the  $\text{NO}^+$  and O fragments. This distribution is shown in Figure 4b.

**B. Energy-Selected Photoelectron Transients and Polarization.** To study in more detail the origin of the oscillations in the photoelectron transients, we measured the electron transients for selected energy regions by using a mask on the fiber-optic window. We used two different masks, one mask was made such that only light from very slow (about 0 eV) photoelectrons at the center of the image would pass and reach the PMT. A second mask was made such that only light from a small circular

rim at a radius corresponding to photoelectrons with a kinetic energy of about 0.88 eV would pass. In the top panel of Figure 5 the photoelectron transient is shown for 0 eV photoelectrons and pump–probe delays up to 4 ps. As can be observed, the trace shows (somewhat irregular) oscillations superimposed on an exponential decaying signal. Note that near zero delay time the signal is clipped and saturated at the detector so that the modulations can be observed more clearly. The polarizations of both the 400 and 266 nm laser pulses were linear and parallel to the plane of the detector. To analyze the period of the oscillations, we have fitted an exponential curve through the transient and subtracted this curve from the smoothed data. The resulting difference signal is shown in the middle panel of Figure 5 and the fast Fourier transform (FFT) is given in the bottom panel of Figure 5. The dominant oscillation period is about 750 fs, which corresponds to an energy of about  $43 \text{ cm}^{-1}$ .

In the top panel of Figure 6 the photoelectron transient is shown for the fast (0.88 eV) photoelectrons and similar laser polarizations. For these faster electrons much more regular and distinct oscillations are observed. As was done for the slow electrons, an exponential fit to the overall decay was subtracted from the smoothed signal and shown in the middle panel of Figure 6, with the resulting FFT in the bottom panel of Figure 6. For the 0.88 eV electrons the dominant oscillation period is about 590 fs, which corresponds to an energy spacing of about  $57 \text{ cm}^{-1}$ . Some smaller peaks are observed in the FFT spectrum at lower frequency. We believe that they are artifacts due to the lower signal-to-noise ratio of the oscillatory pattern at pump–probe time delays between 2 and 4 ps. If we do the FFT (not shown here) only for the part of the transient from 0 to 2 ps, these smaller peaks disappear and only the strong peak with a period of about 590 fs remains.

In Figure 7 we show three transients for masked photoelectrons of 0.88 eV where the linear polarization of the 400 nm pump laser was set at three different angles with respect to the polarization of the linear probe laser, which was in the plane of

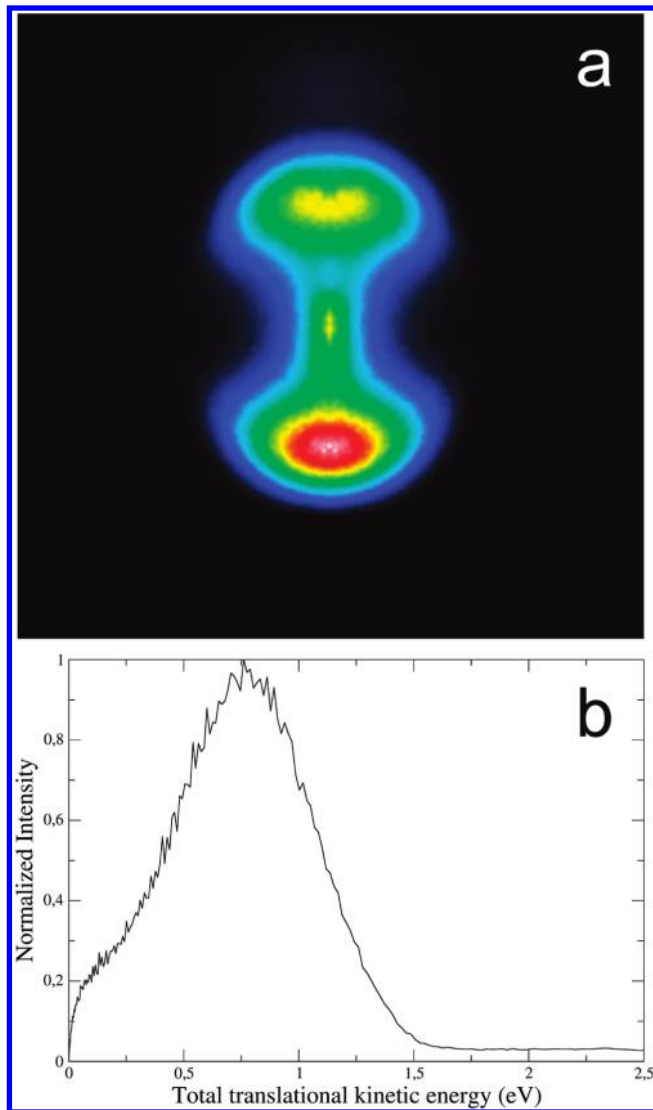


**Figure 4.** (a) Velocity map ion image of the NO<sup>+</sup> fragment recorded at the peak of the cross-correlation between the 400 and 266 nm laser pulses. Polarizations of the pump and probe laser beams are parallel to each other and to the surface of the imaging detector. The up-down asymmetry in intensity is probably due to some inhomogeneity in the detection system. The imaging plane is parallel to the velocity direction of the molecular beam. This center-of-mass velocity of NO<sub>2</sub> in the molecular beam displaces the actual NO<sup>+</sup> image from the center of the image. For the Abel inversion the image is shifted such that the lobes of the NO<sup>+</sup> fragment are centered well. There is some background in the vacuum chamber being ionized at the position where the two lasers cross, and this gives a weak spot of ion signal near the upper part of the NO<sup>+</sup> recoil (in the original unshifted image this spot is in the center of the image where the lasers cross). This weak spot of background ions can be ignored for the further discussion and conclusions of this paper. (b) Kinetic energy release of the NO<sup>+</sup> fragment obtained at 0 fs delay time with 400 nm pump and 266 nm probe wavelengths. The distribution was derived from the Abel-inverted image from Figure 4a.

the CCD detector. In Figure 7a the polarization of the 400 nm pump laser was parallel, in Figure 7b the 400 nm polarization was set at 55° out of the plane of the CCD detector, and in Figure 7c the 400 nm pump polarization is perpendicular to the plane of the CCD detector, i.e., along the TOF axis. The vertical axis of the three transients can be compared directly, as no change in settings of the PMT detector were made, for the linear geometry, panel a, the enhancement is strongest near 0 fs time and the detector gain was such that the signal was

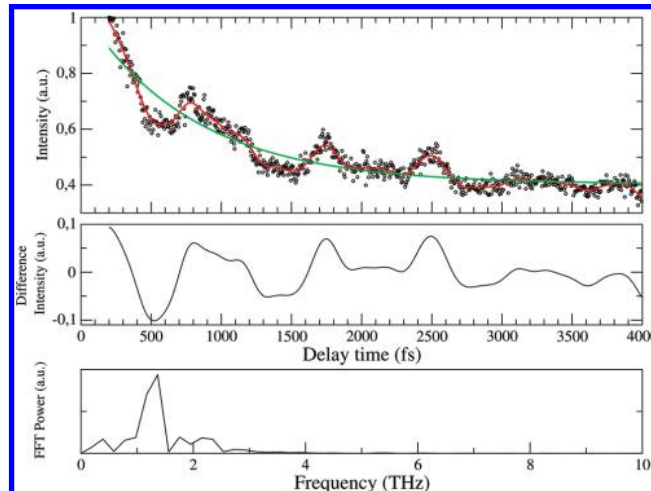


**Figure 5.** Pump-probe transients for selected photoelectrons with near zero kinetic energy obtained with 400 nm pump and 266 probe wavelengths. The slow photoelectrons were selected by masking the output of the fiber optic window such that light from the phosphor of only the small spot in the middle of the image was detected by the PMT. (a) Transient and fitted exponential decay. (b) Smoothed experimental data where the fitted exponential of panel a is subtracted. (c) Power spectrum of the FFT of the experimental oscillations shown in panel b.

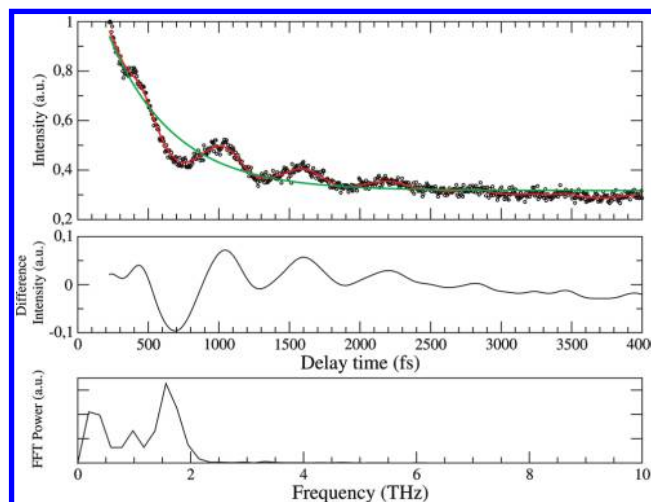


**Figure 6.** Pump-probe transients for selected photoelectrons with 0.88 eV kinetic energy obtained with 400 nm pump and 266 probe wavelengths. The fast photoelectrons were selected by masking the output of the fiber-optic window such that light from the phosphor of only the rim of the image corresponding to these fast photoelectrons (see also Figure 2c) was detected by the PMT. (a) Transient and fitted exponential decay. (b) Smoothed experimental data where the fitted exponential of panel a is subtracted. (c) Power spectrum of the FFT of the experimental oscillations shown in panel b. The smaller peak near low frequencies of 0.3 THz is not physical but due to an insufficient signal-to-noise ratio of the photoelectron signal at time delays between 2 and 4 ps (see also the text).

satürating; see the somewhat rounded and flat signal near 0 fs. However, at all three geometries the oscillations are clearly observed even though the modulation contrast becomes somewhat weaker when the angle between the two polarizations becomes larger.

In Figure 8 we show three transients for masked photoelectrons of 0.88 eV where the polarization of the 266 nm probe laser was circular and the polarization of the 400 nm pump laser was changed from linear (parallel to the CCD detector plane), panel a, to circular, panel b, and perpendicular in panel c, i.e., again linear but along the TOF axis. The vertical axis of the

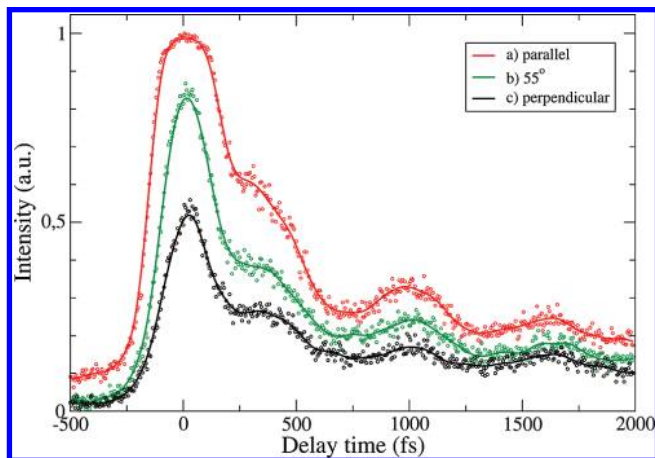


**Figure 7.** Pump–probe transients for selected photoelectrons with 0.88 eV kinetic energy obtained with 400 nm pump and 266 nm probe wavelengths and masking the output of the fiber optic window. The transients are shown for three different pump–probe polarization geometries with the linear polarization of the 266 nm probe laser fixed and parallel to the CCD image plane: (a) 400 nm pump laser linear polarization and parallel to the polarization of the 266 nm probe laser; (b) 400 nm pump laser linear polarization and at 55° to the polarization of the 266 nm probe laser; (c) 400 nm pump laser linear polarization and at 90° (perpendicular) to the polarization of the 266 nm probe laser.

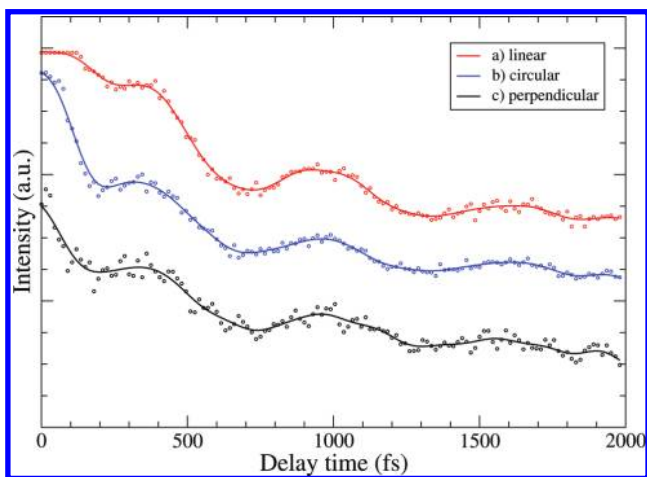


**Figure 8.** Pump–probe transients for selected photoelectrons with 0.88 eV kinetic energy obtained with 400 nm pump and 266 nm probe wavelengths and masking the output of the fiber optic window. The transients are shown for three different pump–probe polarization geometries with the circular polarization of the 266 nm probe laser fixed and the propagation direction parallel to the CCD image plane: (a) 400 nm pump laser linear polarization and parallel to the CCD image plane; (b) 400 nm pump laser circular polarization and the propagation direction parallel to the CCD image plane; (c) 400 nm pump laser linear polarization and perpendicular to the CCD image plane.

three transients can be compared directly, as no changes in settings of the PMT detector were made; however, panel c, was taken a day later than the data of panels a and b. Again, at all three geometries the oscillations are very clearly observable and perhaps the signal-to-noise is even better compared to the transients where the 266 had linear polarization. We will discuss these transients further in section IV below.

**C. Photoelectron Angular Distribution.** To study in more detail the angular distribution of the photoelectron, we have measured several photoelectron images at various pump–probe delay times. To correct for the photoelectron contributions from both lasers individually, we subtracted from the data a photoelectron image that was taken with the delay time set at large

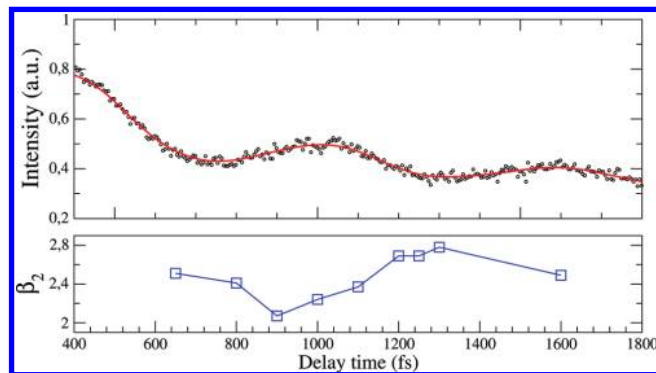


**Figure 9.** Variation of the angular distribution of selected photoelectrons with 0.88 eV kinetic energy. In the top panel the variation of the total photoelectron signal (using the masked electron detection) for both linear and parallel polarization of 400 and 266 nm lasers is repeated. In the bottom panel we show the extracted second Legendre coefficient  $\beta_2$  from the angular distribution of the Abel-inverted images taken at various delay times. The estimated experimental error in  $\beta_2$  from analysis of multiple data files at the same delay time is about 0.1.

negative delay time of about 1–2 ps, i.e., when the 266 nm laser is ahead of the 400 nm laser pulse. The polarization of pump and probe laser were set to be linear and parallel to the detector plane so that the real three-dimensional distribution can be obtained from an Abel-inversion algorithm. From the Abel-inverted electron image, the laboratory frame angular distribution of the ejected photoelectrons,  $I(\theta)$ , as a function of the polar angle  $\theta$  between the laser polarization direction and the recoil  $k$  vector direction of the ejected electrons can be extracted. The photoelectron angular distribution for a selected electron kinetic energy,  $E$ , was fitted to the following expression

$$I(\theta) = \frac{\sigma}{4\pi} [1 + \beta_{2,E} P_2(\cos \theta) + \beta_{4,E} P_4(\cos \theta) + \dots] \quad (3.1)$$

where  $\sigma$  is the total photoionization cross section,  $P_2(\cos \theta)$  and  $P_4(\cos \theta)$  the second- and the fourth-order Legendre polynomials, and  $\beta_{2,E}$  and  $\beta_{4,E}$  the anisotropy parameters. The best fit coefficient for  $E = 0.88$  eV was observed to vary between  $\beta_2 \approx 2$ –2.7 and  $\beta_4 \approx 0.0$ –0.6. Multiple images were taken on different days to estimate the measurement error in  $\beta_2$ , which we extract to be about 0.1. By careful analysis of the images, it was consistently observed that at time delays corresponding to the valleys in the total photoelectron signal the extracted  $\beta_2$  was somewhat larger than the extracted  $\beta_2$  at the peaks of the photoelectron signal; see Figure 9. These measurements were made for time delays within the range of about 600–1600 fs where the oscillations are observed most clearly. We also see some changes in the extracted fourth Legendre coefficient  $\beta_4$  where near 900 fs delay time  $\beta_4 \approx 0.0$  and near 1250–1300 fs  $\beta_4 \approx 0.6$ . We believe that the origin of the  $E = 0.88$  eV electron is a  $(3 + 1')$  excitation (see section IV below), therefore it should be possible in principle to obtain a laboratory frame  $\beta_2$  that exceeds the limiting value of 2 for a parallel one-photon ionization process.

#### IV. Discussion

**A. General Observations.** The origin of the oscillations observed in femtosecond transients of slow photoelectrons and  $\text{NO}^+$  ions was reported and debated by the groups of Whitaker and Soep in two experimental studies. In the first report<sup>7</sup> they suggested that these oscillations may measure the average energy spacing between resonant levels of the  $\text{A}^2\text{B}_2/\text{X}^2\text{A}_1$  states close



to the conical intersection, while in the second study<sup>8</sup> they attributed the oscillations to wave packet motion along a soft coordinate resembling a free rotation of an oxygen atom around a core NO molecule at large O–NO distance. The oscillation period reported in the second paper was about 845 fs, which is close but slightly longer than the value of about 750 fs observed by us for the near 0 eV photoelectrons.

A theoretical study on the periodic oscillations was carried out by Sanrey and Joyeux.<sup>9</sup> They launched wave packets on the excited  $\tilde{A}^2B_2$  electronic state and focused on the evolution at long delay times. They concluded from the results of the wave packet calculations that the angular frequencies of the oscillations are probably related to the energy gaps between states  $[0, \nu_2', 0]$  and  $[1, \nu_2' - 2, 0]$  that are excited at time  $t = 0$ . Another theoretical study was performed by Arasaki and Takatsuka<sup>26</sup> who calculated global potential energy surfaces of the ground and first excited state of NO<sub>2</sub> and the first triplet state of the ion. They performed wave packet calculations including nonadiabatic interaction; however their study did not provide more insight in the origin of the oscillations in the transients of the slow electrons.

One striking difference between the results of Whitaker, Soep, and co-workers and our results is that we observe a very clear fast photoelectron peak at an energy of 0.88 eV. This peak starts to grow in at 300 fs and is completely formed at 400 fs. Such a fast electron peak was not reported by Whitaker, Soep, and co-workers.<sup>7,8</sup>

One of the most extensive and recent femtosecond pump–probe studies of the NO<sub>2</sub> photodynamics was done by Vredenburg et al.<sup>10</sup> employing coincidence imaging of photoelectrons and ions. In agreement with our observations also in the coincidence study a distinct electron peak at 0.88 eV was observed. Vredenburg et al. concluded that nonadiabatic dynamics between the ground state and the  $\tilde{A}^2B_2$  state after absorption of a 400 nm photon was reflected in the transient photoelectron spectrum of the NO<sub>2</sub><sup>+</sup> parent ion. Furthermore, Rydberg states were believed to be used as “stepping” states responsible for the rather narrow and well-separated photoelectron spectra in the NO<sub>2</sub><sup>+</sup> parent ion. At short pump probe delay times, the dominant multiphoton pathway for NO<sup>+</sup> formation was a  $3 \times 400 \text{ nm} + 1 \times 266 \text{ nm}$  excitation ( $3 + 1'$ ). At long delay times (>500 fs) two multiphoton pathways were observed, one pathway was assigned to a  $1 \times 400 \text{ nm} + 2 \times 266 \text{ nm}$  photon excitation ( $1 + 2'$ ) giving rise to very slow electrons and NO<sup>+</sup> ions. A second pathway was attributed to a  $3 \times 400 \text{ nm}$  photon absorption to NO<sub>2</sub> Rydberg states followed by dissociation toward neutral electronically and vibrationally excited NO( $A^2\Sigma$ ,  $\nu = 1$ ) fragments, followed by one 266 nm photon ionization. In the case of the coincidence experiment by Vredenburg et al. they did not observe any clear oscillatory pattern at positive delay times in the pump probe transients. Probably, this absence in the observation was due to a somewhat unfavorable signal-to-noise ratio limited by the experimental conditions demanding a relatively low count rate per laser shot in coincidence imaging experiments.

From about 300 fs toward long delays we observe, see Figure 3, in the photoelectron spectra also the two types of photoelectrons, a peak corresponding to almost zero-kinetic energy electrons and a somewhat stronger electron peak with significant kinetic energy located at 0.88 eV. It was shown by Vredenburg et al. that on the 400 nm pump side there are two competing channels leading to production of NO<sup>+</sup> and the corresponding photoelectrons at 0 or 0.88 eV. To extract the contribution of each of these processes to the total intensity and the oscillatory

pattern of the transient, we must discriminate between these two channels. One way this can be done is by focusing on the electron detection, and we used the simple energy selective masking method to monitor the slow ( $1 + 2'$ ) or the fast ( $3 + 1'$ ) photoelectrons in an independent way. By carefully recording the pump–probe electron transients with the masked detector, we observed that both types of photoelectrons exhibit oscillations but with different periods, about 590 fs for the high kinetic energy component and about 750 fs for the slow component. From the photoelectron spectra the fast electrons seem to dominate over the slow ones and this was mainly the reason why the period of the total overlapped oscillating overall signal was close to about 600 fs.

**B. Oscillatory Mechanism.** In various molecular systems oscillatory wave packet dynamics have been observed due to rotational revivals.<sup>27–31</sup> In fluorescence, ion, or photoelectron detection, revival structures were observed due to the rephasing and dephasing of rotational wave packets created in bound potentials. Time-of-flight mass selected ion detection and fluorescence detection were reported in 1991 in femtosecond pump–probe molecular beam experiments by Dantus et al.<sup>28</sup> on rotational revivals in a rotationally cold molecular beam of the I<sub>2</sub> molecule. Suzuki and co-workers<sup>29,30</sup> created rotational wave packets in the NO( $A^2\Sigma$ ) state and probed the laboratory frame photoelectron angular distribution as a function of pump–probe delay. The authors report no or little dependence of the overall ionization yield on the pump–probe delay time; however, a strong dependence of the angular distribution of the photoelectron with pump–probe delay time was observed. Full angular revivals in diatomics (or linear polyatomics) occur at revival times  $T = 1/(2Bc)$ ,<sup>27</sup> with  $B$  the rotational constant and  $c$  the speed of light. Also partial revivals at  $T/4$ ,  $T/2$ , or  $3T/4$  can be observed due to a partial rephasing of the rotational wave packet, and they were reported for instance for the I<sub>2</sub> molecule.<sup>31</sup>

If the oscillatory dynamics in the transients of photoelectrons from NO<sub>2</sub> photodynamics were due to rotational wave packets, the oscillation periods would be determined by the rotational constant of the molecule. The rotational constant in the ground state of NO<sub>2</sub>,  $B = 0.43 \text{ cm}^{-1}$ , and in the ground state of the NO<sub>2</sub><sup>+</sup> ion,  $B^+ = 0.417 \text{ cm}^{-1}$ .<sup>1,32</sup> For the NO molecule the rotational constant in the excited  $A^2\Sigma$  state is  $1.995 \text{ cm}^{-1}$ . This means full revivals would be spaced at time intervals of  $T \approx 39 \text{ ps}$  (NO<sub>2</sub>) or  $T \approx 8.4 \text{ ps}$  (NO  $A^2\Sigma$ ), and half revivals at about 20 or 4 ps. It is clear that these time scales are much longer than the observed periods of about 590–750 fs. Furthermore, we did extensive polarization experiments for the fast electron as in that case the oscillations were most regular; see Figures 7 and 8. We do see some minor changes in the modulation depth (visibility) of the oscillations with polarization geometry, but generally the laser polarization does not affect the presence of the oscillations significantly. Also when both polarizations of 400 nm pump and 266 nm probe laser are circular, very clear oscillations are observed, see transient b in Figure 8. This is another strong indication that rotational structures, i.e., revivals of angular momentum alignment, do not play a role in the oscillations.

A classic femtosecond pump–probe experiment was performed by Zewail and co-workers<sup>33</sup> on predissociation dynamics in NaI. Oscillatory wave packet dynamics was observed of a quasi-bound movement due to an avoided crossing between the ground state and the first excited state. Extensive theoretical calculations have been performed to reproduce the observed experimental data; for an overview see refs 34 and 35 and references therein.



The coincidence imaging experiment on NO<sub>2</sub> by Vredenberg et al.<sup>10</sup> has given a clear insight in the multiphoton mechanism for the formation of the 0.88 eV photoelectron channel in coincidence with NO<sup>+</sup>. This channel is due to a three-photon excitation at 400 nm followed by dynamics and subsequently probed by a time-delayed one-photon 266 nm probe excitation.

The mechanism that we propose (see below) to be responsible for the oscillations in the transients of the 0.88 eV photoelectron after photoexcitation of the NO<sub>2</sub> molecule with 400 nm fs laser pulses was arrived at by comparison with earlier reported theoretical potential energy curves of the Rydberg states of NO<sub>2</sub>.<sup>36</sup> In that earlier work, the potential energy curves corresponding to geometries of different point group symmetry were not comparable as they had been calculated by solutions of different secular equations. For this reason, in the present work, extending our earlier theoretical calculations,<sup>36</sup> new ab initio multireference single and double substitution configuration interaction (MRDCI) calculations<sup>37–39</sup> have been carried out on Rydberg states of NO<sub>2</sub>, relevant to the present experimental work, at symmetric and asymmetric linear and symmetric bent geometries. As mentioned, the object of the present work is to calculate the potential energy surfaces of the lower Rydberg states, using improved configuration interaction spaces in order to be able to represent consistently (i.e., on the same energy scale) cuts through the potential energy surfaces at different geometries and symmetries. The identical basis set as previously has been employed,<sup>36</sup> consisting of the [11s6p/5s3p] basis sets of Dunning<sup>40</sup> for oxygen and nitrogen, where the nitrogen basis set was augmented for the present calculations with s, p, and d diffuse functions, with exponents 0.028, 0.0066, and 0.0032 for the s, 0.025 and 0.0051 for the p, and 0.015 and 0.0032 for the d functions. Furthermore, a single d polarization function with exponent 0.88 was included in both the oxygen and the nitrogen basis sets. The equilibrium geometry of the ground state of NO<sub>2</sub> is bent and of <sup>2</sup>A<sub>1</sub> symmetry in the C<sub>2v</sub> point group symmetry. At linear symmetric geometries with D<sub>∞h</sub> (D<sub>2h</sub> for the calculations) symmetry the ground state is <sup>2</sup>Π<sub>u</sub> (<sup>1</sup>2B<sub>2u</sub> + <sup>1</sup>2B<sub>3u</sub> in D<sub>2h</sub> point group), correlating with X<sup>2</sup>A<sub>1</sub> + A<sup>2</sup>B<sub>1</sub> of bent symmetric NO<sub>2</sub>. Linear asymmetric dissociation corresponds to C<sub>∞v</sub> point group symmetry, which in the calculations is reduced to C<sub>2v</sub>. In addition to the calculations employing the above symmetry groups, namely, C<sub>2v</sub> (for bent symmetric and linear asymmetric geometries) and D<sub>2h</sub> for linear symmetric geometries, all the calculations have been carried out in C<sub>s</sub> point group symmetry as well, employing the same computational conditions throughout, to ensure comparability and consistency of the different cross sections of the potential energy hypersurfaces. For the purposes of the present experimental work, the new calculations involve the bending potential energy curves of the <sup>2</sup>A<sub>1</sub> states of NO<sub>2</sub>, the linear symmetric dissociation of the <sup>2</sup>A<sub>g</sub> (i.e., <sup>2</sup>Σ<sub>g</sub><sup>+</sup> and <sup>2</sup>Δ<sub>g</sub>) states and the linear asymmetric dissociation of the <sup>2</sup>A<sub>1</sub>(<sup>2</sup>Σ<sup>+</sup> and <sup>2</sup>Δ) states. Larger reference spaces and lower selection thresholds<sup>37–39</sup> have been employed in the present work than previously,<sup>36</sup> as allowed by the increased present-day computational capabilities. The size of the reference spaces are 135 configuration functions and 9 roots (C<sub>2v</sub> bending), 260 and 9 (C<sub>2v</sub> asymmetric dissociation), 157 and 7 (D<sub>2h</sub> geometries), and 286 configuration functions and 13 roots for the C<sub>s</sub> calculations. The corresponding CI spaces varied between 400000 and 700000 configuration functions.

Further computational details and full results of the new calculations on the electronic states of NO<sub>2</sub> will be presented elsewhere. Here, for brevity, only the results on the states relevant to the present experimental work are presented in Figure

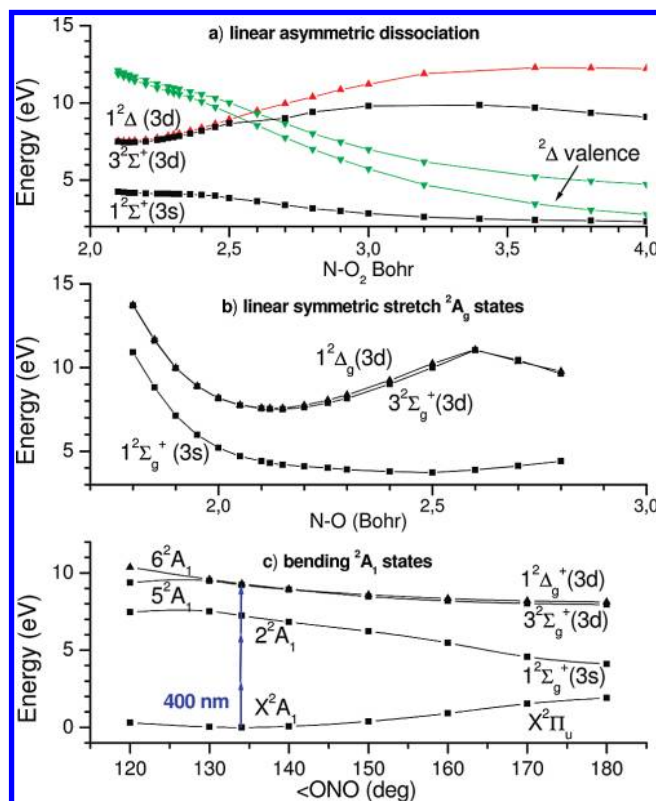


**Figure 10.** Potential energy curves calculated for different geometries as a function of asymmetric dissociation coordinate, symmetric stretch coordinate, and bending angle coordinate. The figures result from new and improved MRDCI calculations (see text) as compared to calculations reported previously.<sup>36</sup> (a) Linear asymmetric N–O<sub>(2)</sub> dissociation potentials at a fixed distance of the other bond N–O<sub>(1)</sub> of 2.12 bohr. (b) Symmetric stretch potentials as a function of the N–O distance obtained from D<sub>2h</sub> calculations. (c) Symmetric bending potentials of the relevant <sup>2</sup>A<sub>1</sub> surfaces at the equilibrium N–O distance of the X<sup>2</sup>A<sub>1</sub> ground state of 2.2552 bohr. At the equilibrium angle of 134°, we added the three arrows representing the 400 nm pump laser three photon excitation path of 3 × 3.1 eV = 9.3 eV total excitation.

10. In the lower panel (c) four totally symmetric <sup>2</sup>A<sub>1</sub> bending states are shown as a function of the ONO bending angle at a NO distance of 2.2552 bohr, the equilibrium distance of the ground state of NO<sub>2</sub>. In this panel we indicated with the blue arrows the total excitation energy of 9.3 eV (3 × 400 nm pump photons) from the equilibrium bending angle of 134° of ground state NO<sub>2</sub>. It appears from the calculations that at 9.3 eV two totally symmetric potentials are in resonance, the <sup>5</sup>2A<sub>1</sub> state which correlates to the <sup>3</sup>2Σ<sub>g</sub><sup>+</sup>(3d) Rydberg state at linear geometry, and the <sup>6</sup>2A<sub>1</sub> state which correlates to the <sup>1</sup>2Δ<sub>g</sub>(3d) Rydberg state at linear geometry. In the top panel (a) relevant Rydberg states and valence states are given for a linear NO<sub>2</sub> molecule as a function of the (asymmetric) N–O<sub>2</sub> dissociation distance with the other (bound) N–O<sub>1</sub> distance equal to 2.12 bohr, the equilibrium distance of the linear ground state of the NO<sub>2</sub><sup>+</sup> ion. In the middle panel (b) the same potentials are shown for symmetric N–O stretch motion in linear <sup>2</sup>A<sub>g</sub> symmetry.

The mechanism that we propose to be responsible for the oscillations in the transients of the 0.88 eV photoelectron after photoexcitation of the NO<sub>2</sub> molecule with 400 nm fs laser pulses may be similar to the electronic predissociation mechanism that was observed for the diatomic NaI molecule. In panel a of Figure 10 we see that the bound <sup>1</sup>2Δ<sub>g</sub>(3d) Rydberg state is crossed by two dissociative valence states of <sup>2</sup>Δ symmetry. In fact this will lead to avoided crossings, or in multiple dimensions conical intersections. The location of the first avoided crossing is just

near 9.0 eV. We think that the three-photon excitation creates initially a localized wave packet in this quasi-bound potential. It starts after excitation from the NO<sub>2</sub> Franck–Condon geometry near 134° to bend toward linear geometry. It will subsequently move along the multidimensional surfaces and may partially predissociate via the conical intersection with the  $^2\Delta$  valence states. The  $5^2A_1$  and  $6^2A_1$  states are nearly degenerate (the new calculations show that the energy difference is within 660 cm<sup>-1</sup> for excitation from the equilibrium geometry of the NO<sub>2</sub> ground state); it is likely we create excitation on both  $5^2A_1$  and  $6^2A_1$  surfaces. Interestingly, we observe in the time-delayed photoelectron spectra, see Figure 3, that at relatively early times of 200–300 fs, the shape of the photoelectron peak near 0.88 eV is rather broad. In fact it looks as if the peak consists of two peaks separated by some 0.078 eV (630 cm<sup>-1</sup>). This energy difference is very similar to the calculated energy difference of 660 cm<sup>-1</sup> between the  $5^2A_1$  and  $6^2A_1$  states. When the time delay is increased to 800–1000 fs the higher energy shoulder disappears and a more normal narrow photoelectron peak is observed near 0.88 eV. The  $5^2A_1\ 3^2\Sigma_g^+(3d)$  state is also crossed by a dissociative valence state. So, we think that the wave packet created by the 400 nm pump pulse will oscillate with changing Rydberg and valence character and this oscillating character is being probed in ionization by the 266 nm probe pulse. This leads to time delays with (slightly) enhanced creation of NO<sup>+</sup> + 0.88 eV photoelectron and time delays with slightly less efficient ionization. It appears that after some 3–5 ps the wave packet has finally spread and decayed such that a constant and finite amount of NO(3s A<sup>2</sup>Σ) is created that is ionized by the 266 nm probe pulse giving a photoelectron of 0.88 eV.

It is clear that a full picture of the precise time scales and more complete interpretation of the oscillatory character can only be obtained after more extensive theoretical calculations modeling the initial excitation on the relevant potential energy surfaces. A multidimensional (bending, symmetric, and asymmetric stretch) calculation needs to be done in combination with nonadiabatic interaction to evaluate the time scale and precise character of the wave packet evolution and predissociation. We hope that these multidimensional dynamical calculations will be performed in the future on high-quality potential energy surfaces.

With respect to the somewhat more irregular oscillations observed for the slow photoelectron our experiment does not provide much more insight. It is clear that the formation mechanism is a one-photon 400 nm excitation followed by a two-photon ionization by the 266 nm probe pulse ( $2 \times 266\text{ nm} = 3 \times 400\text{ nm} = 9.3\text{ eV}$ ) leading to very slow photofragments and near zero photoelectrons. However, after one-photon excitation at 400 nm there is also rapid nonadiabatic interaction between the  $\tilde{A}^2B_2$  state and the electronic ground state  $\tilde{X}^2A_1$ .<sup>9,26</sup> Vredenburg et al. discussed this nonadiabatic interaction and suggested that this was responsible for the rapid decrease of a photoelectron peak at 0.4 eV in coincidence with the NO<sub>2</sub><sup>+</sup> ion.

## V. Conclusions

In this paper we have reported femtosecond pump–probe spectroscopy in combination with ion and electron imaging to study oscillatory wave packet dynamics in NO<sub>2</sub> photodynamics. We have employed spatially masked photoelectron imaging to measure the pump–probe transients of energy selected photoelectron channels. This masking technique makes it possible to obtain pump–probe transients with high signal-to-noise ratio with relatively modest measurement duration. Distinct oscillatory patterns are observed in the transients up to several

picooseconds for both the slow (near 0 eV) and the fast (near 0.88 eV) photoelectrons. The oscillation pattern for the two electron channels is different with typical periods of about 750 fs (slow electrons) and 590 fs (fast electrons). Extensive polarization experiments are performed with both linear and circular polarized pump and probe polarizations. Clear oscillations are observed in all geometries. The time scale of the oscillations and the polarization experiments exclude rotational wave packets in NO<sub>2</sub> or NO as the origin of the oscillations. New ab initio calculations are performed of the electronic states in NO<sub>2</sub> of both Rydberg and valence type character. The calculations show that there are avoided crossings or conical intersections between bound and dissociative excited states of different Rydberg and valence character near 9 eV. We propose that an oscillating and predissociating wave packet in a quasi-bound potential of mixed character may explain the oscillations observed in the total photoelectron yield in the fast channel near 0.88 eV. More complete dynamical calculations on multidimensional surfaces need to be performed to give a more quantitative comparison and interpretation of the experimentally observed photoelectron oscillations.

**Acknowledgment.** This research has been financially supported by the council for Chemical Sciences of the Dutch Organization for Scientific Research (NWO-CW).

## References and Notes

- (1) Delon, A.; Jost, R. *J. Chem. Phys.* **1991**, *95*, 5686.
- (2) Biesheuvel, C. A.; Bulthuis, J.; Janssen, M. H. M.; Stolte, S.; Snijders, J. G. *J. Chem. Phys.* **1998**, *109*, 9701.
- (3) Joyeux, M.; Jost, R.; Lombardi, M. *J. Chem. Phys.* **2003**, *119*, 5923.
- (4) Singhal, R. P.; Kilic, H. S.; Ledingham, K. W. D.; Kosmidis, C.; McCann, T.; Langley, A. J.; Shaikh, W. *Chem. Phys. Lett.* **1996**, *253*, 81.
- (5) Davies, J. A.; LeClaire, J. E.; Continetti, R. E.; Hayden, C. C. *J. Chem. Phys.* **1999**, *111*, 1.
- (6) Lopez-Martens, R. B.; Schmidt, T. W.; Roberts, G. *J. Chem. Phys.* **1999**, *111*, 7183.
- (7) Eppink, A. T. J. B.; Whitaker, B. J.; Gloaguen, E.; Soep, B.; Coroiu, A. M.; Parker, D. H. *J. Chem. Phys.* **2004**, *121*, 7776.
- (8) Form, N. T.; Whitaker, B. J.; Poisson, L.; Soep, B. *Phys. Chem. Chem. Phys.* **2006**, *8*, 2925.
- (9) Sanrey, M.; Joyeux, M. *J. Chem. Phys.* **2007**, *126*, 074301.
- (10) Vredenburg, A.; Roeterdink, W. G.; Janssen, M. H. M. *J. Chem. Phys.* **2008**, *128*, 204311.
- (11) Vredenburg, A.; Roeterdink, W. G.; Janssen, M. H. M. *Rev. Sci. Instrum.* **2008**, *79*, 063108.
- (12) Janssen, M. H. M.; Parker, D. H.; Sitz, G. O.; Stolte, S.; Chandler, D. W. *J. Phys. Chem.* **1991**, *95*, 8007.
- (13) Mueler, J. A. S.; Rogers, A.; Houston, P. L. *J. Phys. Chem.* **1998**, *A 102*, 9666.
- (14) Goncharov, V.; Herath, N.; Arrequi, A.; Banares, L.; Suits, A. G. *J. Phys. Chem. A* **2009**, *113*, 3840.
- (15) Sztaray, B.; Baer, T. *Rev. Sci. Instrum.* **2003**, *74*, 3763.
- (16) Roeterdink, W.; Rijs, A. M.; Bazalgette, G.; Wasylczyk, P.; Wiskerke, A.; Stolte, S.; Drabbels, M.; Janssen, M. H. M. In *Atomic and Molecular Beams: The State of the Art 2000*; Campargue, R. C., Ed.; Springer-Verlag: Berlin and Heidelberg, 2001; Chapter III-8.
- (17) Roeterdink, W. G.; Janssen, M. H. M. *Chem. Phys. Lett.* **2001**, *345*, 72.
- (18) Roeterdink, W. G.; Janssen, M. H. M. *Phys. Chem. Chem. Phys.* **2002**, *4*, 601.
- (19) Rijs, A. Ph.D. thesis, Vrije Universiteit, Amsterdam, 2003.
- (20) Irimia, D.; Kortekaas, R.; Janssen, M. H. M. *Phys. Chem. Chem. Phys.* **2009**, *11*, 3958.
- (21) Irimia, D.; Dobrikov, D.; Kortekaas, R.; Voet, H.; van den Ende, D. A.; Groen, W. A.; Janssen, M. H. M. *Rev. Sci. Instrum.* **2009**, *80*.
- (22) Lipciuc, M. L.; van den Brom, A. J.; Dinu, L.; Janssen, M. H. M. *Rev. Sci. Instrum.* **2005**, *76*, 123103.
- (23) Lipciuc, M. L.; Janssen, M. H. M. *Phys. Chem. Chem. Phys.* **2006**, *8*, 3007.
- (24) Brandi, F.; Velchev, I.; Hogervorst, W.; Ubachs, W. *Phys. Rev.* **2001**, *A 64*, 032505.
- (25) Kruit, P.; Kimman, J.; Muller, H. G.; van der Wiel, M. J. *Phys. Rev.* **1983**, *A 28*, 248.

- (26) Arasaki, Y.; Takatsuka, K. *Chem. Phys.* **2007**, *338*, 175.
- (27) Felker, P. M.; Baskin, J. S.; Zewail, A. H. *J. Phys. Chem.* **1986**, *90*, 724.
- (28) Dantus, M.; Janssen, M. H. M.; Zewail, A. H. *Chem. Phys. Lett.* **1991**, *181*, 281.
- (29) Tsubouchi, M.; Suzuki, T. *J. Chem. Phys.* **2004**, *121*, 8846.
- (30) Suzuki, T. *Annu. Rev. Phys. Chem.* **2006**, *57*, 555.
- (31) Rosca-Pruna, F.; Vrakking, M. J. J. *Phys. Rev. Lett.* **2001**, *87*, 153902.
- (32) Jarvis, G. K.; Song, Y.; Ng, C. Y.; Grant, E. R. *J. Chem. Phys.* **1999**, *111*, 9568.
- (33) Mokhtari, A.; Cong, P.; Herek, J. L.; Zewail, A. H. *Nature* **1990**, *348*, 225.
- (34) Cong, P.; Roberts, G.; Herek, J. L.; Mokhtari, A.; Zewail, A. H. *J. Phys. Chem.* **1996**, *100*, 7832.
- (35) Marquet, P.; Engel, V. *Phys. Chem. Chem. Phys.* **2005**, *7*, 469.
- (36) Petsalakis, I. D.; Theodorakopoulos, G.; Child, M. S. *J. Chem. Phys.* **2001**, *115*, 10394.
- (37) Buenker, R. J. In *Studies in Physical and Theoretical Chemistry, Current Aspects of Quantum Chemistry*; Carbo, R., Ed.; Elsevier: Amsterdam, 1981; Vol.2, p 17.
- (38) Buenker, R. J.; Philips, R. A. *THEOCHEM* **1985**, *123*, 291.
- (39) Buenker, R. J.; Krebs, S. In *Recent Advances in Multireference Methods*; Hirao, K., Ed.; World Scientific: Singapore, 1999; p 1.
- (40) Dunning, T. H. *J. Chem. Phys.* **1971**, *55*, 716.

JP909031P